RSC Advances

PAPER

View Article Online
View Journal | View Issue

Cite this: *RSC Adv.*, 2017, 7, 39147

Tunable high-κ $Zr_xAl_{1-x}O_y$ thin film dielectrics from all-inorganic aqueous precursor solutions†

K. N. Woods, E. C. Waddington, C. A. Crump, E. A. Bryan, T. S. Gleckler, M. R. Nellist, B. A. Duell, D. P. Nguyen, S. W. Boettcher and C. J. Page*

Received 29th July 2017
Accepted 31st July 2017

DOI: 10.1039/c7ra08362a

rsc.li/rsc-advances

Zirconium oxide has received considerable attention as a dielectric component for microelectronic applications. However, crystallization at relatively low temperatures results in the formation of grain boundaries and high leakage current densities. Doping ZrO_y with Al is known to suppress crystallization, but the effects of Al incorporation on dielectric properties has not been investigated over the complete range of Zr : Al compositions in $Zr_xAl_{1-x}O_y$ (ZAO). Herein, we report an aqueous, all-inorganic route to amorphous high-κ ZAO thin film dielectrics with varying Zr : Al composition. ZAO thin films were spin-cast and annealed at temperatures between 200 and 600 °C to produce dense, uniform, and smooth films with sub-nm roughness. In general, Zr-rich films had higher dielectric constants, ranging from 18.6 for pure ZrO_y to 5.4 for pure AlO_y (1 kHz), while Al-rich films had lower leakage current densities. Of the compositions studied, $Zr_{0.75}Al_{0.25}O_y$ films displayed the optimal balance of dielectric properties and low leakage current densities, making them promising candidates for microelectronic devices.

Introduction

Metal oxide thin films function as critical components in a number of technological applications, including as gate dielectrics in transistors.[1,2] For these applications, amorphous high-κ materials are desirable for lowering power consumption and decreasing leakage current through the dielectric layer.[3] Zirconium oxide (ZrO_y)[4–14] and aluminum oxide (AlO_y)[15–33] are two high-κ materials that have been investigated as alternatives to SiO_2 gate dielectrics. ZrO_y has a high dielectric constant (~25) but is incompatible with the processing temperatures required for integrated circuit manufacturing.[3] This stems from an inherently low crystallization temperature (<500 °C), which leads to grain boundaries and undesirable leakage currents.[34] Additionally, facile diffusion of oxygen through ZrO_y at elevated temperatures can result in uncontrolled interfacial growth at ZrO_2–Si interfaces.[3] Although AlO_y has a lower dielectric constant (~10), it remains amorphous until much higher temperatures (~800 °C) and exhibits high thermodynamic stability on Si.[3]

Previous reports of high-κ zirconium aluminum oxide ($ZrAlO_y$, ZAO) thin film dielectrics indicate that Al incorporation can effectively suppress the crystallization of ZrO_y.[35–42] These reports utilized both vapor phase deposition routes (pulsed laser deposition[35,36] and atomic layer deposition[37,38]) and solution deposition routes (spray pyrolysis[39,40] and sol–gel[41,42]). Solution deposition routes are attractive because they generally employ inexpensive precursors and equipment, allow for facile variation of metal composition, and offer the promise of low-temperature processing.[43,44] However, the previously reported solution deposition routes to ZAO films make use of organic ligands and solvents, which are often difficult to remove and can result in carbon impurities that can adversely affect dielectric properties.[45,46] Only one previous study has investigated the effects of Zr : Al composition on dielectric properties. This study examined a limited composition range using a pyrosol method, but the authors were unable to establish a relationship between composition and dielectric properties.[39]

Herein, we report an all-inorganic aqueous solution deposition route to $Zr_xAl_{1-x}O_y$ (ZAO, $0 \le x \le 1$) thin films. This route is distinct from the previously employed solution deposition routes in that no organic ligands or additives are employed. This all-inorganic aqueous synthetic approach has previously produced dense, ultra-smooth metal oxide dielectric films with a variety of metal components.[34,47–57] Aqueous solution deposition allows for precise control of film composition through the facile manipulation of precursor stoichiometry,[58] which we exploit to investigate a complete range of Zr : Al compositions. The ZAO films prepared *via* this aqueous route are smooth, dense, and defect-free. Films annealed at temperatures ≤500 °C are amorphous when the Al content is ≥10%. Device testing of ZAO-based metal-insulator-semiconductor (MIS) capacitors shows that the dielectric and leakage current density characteristics can be systematically tuned by varying the Zr : Al composition. The facile control of film composition and corresponding electrical properties

---

Department of Chemistry and Biochemistry, Materials Science Institute, University of Oregon, Eugene, OR 97403, USA. E-mail: cpage@uoregon.edu

† Electronic supplementary information (ESI) available: Fourier transform infrared (FTIR) spectra, X-ray reflectivity (XRR) data and best fit models, film thicknesses and densities from XRR best fit models, dielectric constant dispersion data. See DOI: 10.1039/c7ra08362a

make ZAO films promising functional components for microelectronic applications.

Experimental

Precursor solution preparation

A 1.0 M Zr stock solution was prepared by adding $ZrO(NO_3)_2 \cdot xH_2O$ (Sigma Aldrich, 99%) to 18.2 MΩ cm Millipore H_2O heated to ~70 °C. The solution was stirred vigorously for 1 h at this temperature, then stirred overnight at RT to produce a stable solution. A separate 1.0 M Al stock solution was prepared by dissolving $Al(NO_3)_3 \cdot 9H_2O$ (Alfa Aesar, 98.0–102.0%) in 18.2 MΩ cm H_2O at RT and stirring vigorously for 1 h. Mixed ratio precursor solutions were prepared from the 1.0 M stock solutions for a range of Zr : Al ratios. The total metal concentration for all Zr : Al ratios was 1.0 M, and all solutions were filtered through a 0.45 μm PTFE syringe filter.

Thin film preparation

Si substrates (2×2 cm^2 squares) were sonicated in 5% Contrad-70 solution (Decon Laboratories) at RT for 1 h followed by rinsing with 18.2 MΩ cm H_2O. Precursor solutions were deposited onto treated Si substrates through 0.2 μm PTFE filters and then spun at 3000 rpm for 30 s. For samples annealed at or below 500 °C, samples were immediately transferred to a hotplate at 50 °C. Samples were then ramped to 200, 300, 400, or 500 °C (12.5 °C min^{-1}) and held for 1 h. Stacked, two-coat films (used for FTIR, SEM, and impedance measurements) were annealed to 200, 300, 400, or 500 °C for 10 min between coats with a final anneal at the desired temperature for 1 h. The maximum temperature that the hotplates could achieve was 500 °C. Therefore, samples with a final annealing temperature >500 °C were first ramped to 500 °C for 10 min on a hotplate (for each layer), cooled to RT, and then transferred to a box furnace, which was then ramped to the desired final annealing temperature and held for 1 h.

In the case of Al-rich ZAO films ($Zr_xAl_{1-x}O_y$ where $x \leq 0.15$), sonicated Si substrates were also subjected to a 10 min O_2/N_2 plasma etch using a PE-50 Benchtop Plasma Cleaner (Plasma Etch, Inc.) set to maximum power, followed by rinsing with 18.2 MΩ cm H_2O. Following deposition, these Al-rich samples were transferred to hotplates preheated to 150 °C instead of 50 °C. These modifications were necessary to ensure good substrate wettability and to prepare high-quality, Al-rich ZAO films. All other annealing parameters (ramp rate, final annealing time) were kept the same.

Precursor solution characterization

Bulk powders were prepared for thermogravimetric analysis (TGA) from 1.0 M precursor solutions that were dried at 50 °C for 12 h. TGA was done using a TA Instruments Q500A with a ramp rate of 5 °C min^{-1} under an N_2 atmosphere.

Thin film characterization

Fourier transform infrared (FTIR) spectra were collected using a Nicolet 6700 spectrometer in transmission mode. Samples were deposited on lightly doped double-sided polished p-type Si substrates and background subtraction was done using a spectrum collected from a blank Si substrate (heated to match the thermal processing of each measured sample).

X-ray reflectivity (XRR) and grazing incidence X-ray diffraction (GIXRD) measurements were performed using a Rigaku SmartLab diffractometer with a Cu Kα radiation source (40 kV, 44 mA). XRR data were modeled using BedeREFS v4.00 software package,[59] and film thickness and density were extracted from best fit models (see ESI†).

Atomic force microscopy (AFM) images were collected using a Dimension ICON AFM (Bruker, USA) in tapping mode. Standard tapping mode probes were used (42 N m^{-1}, 320 kHz). Images were collected at a scan rate of 1 Hz with 384 lines and 384 measurements per line. Image processing was performed using NanoScope Analysis 1.50 software, and a first order flattening compensated for any sample tilt in each image.

Cross-sectional scanning electron microscopy (SEM) was done using a FEI Helios Dual Beam FIB (5.0 keV accelerating voltage, 86 pA current, immersion mode). Samples were coated with thermally evaporated Al prior to imaging to prevent charging effects.[60]

MIS device fabrication and testing

Metal-insulator-semiconductor (MIS) devices were prepared by thermally evaporating Al top contacts (0.013 cm^2, 100 nm thick) onto ZAO films deposited on degenerately-doped n-type Si substrates (<0.005 Ω cm). Electrical contact to the Si substrate was achieved by physically scratching the film with a scribe and applying an In/Ga eutectic. Impedance measurements were taken using an Agilent 4284A Precision LCR meter at 0.1, 1, and 10 kHz with 500 mV oscillation amplitude. Batch-to-batch variations were evaluated by making three separate samples per annealing temperature and measuring impedance of five MIS devices per sample. A Keithley 2400 SourceMeter (0.2 V steps, 0.2 s delay) was used for current density–electric field (*J*–*E*) characterization. All MIS device testing was performed in ambient atmosphere in a dark environment.

Results and discussion

The decomposition of bulk precursor powders to the corresponding oxides was investigated by TGA (Fig. 1). Mass loss events can be related to the elimination of water and nitrate counterions from the bulk precursor powders (Fig. 1a). The temperatures at which significant mass loss occurs can be better visualized by examining the mass loss derivatives (Fig. 1b). In the case of the ZrO_y precursor, gradual mass loss is observed between 50 and 150 °C (predominately water loss) followed by two large mass loss events between 150 °C and 250 °C (predominantly nitrate loss). Above 250 °C there is gradual mass loss (further water and nitrate loss) until ~500 °C when final densification and crystallization occurs. In contrast, the AlO_y precursor fully condenses and densifies at a much lower temperature, and mass loss appears to be complete by

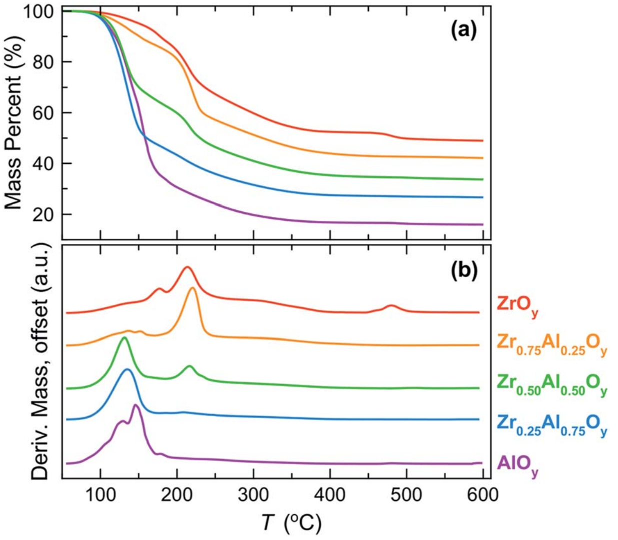

Fig. 1 (a) Mass loss percent and (b) derivative of mass loss (absolute values) as a function of annealing temperature for bulk ZAO precursor powders.

~350 °C with the largest mass losses occurring between 50 and 200 °C.

For the mixed ZAO precursor powders, increasing the Al content decreases both the decomposition temperature and the resulting oxide formation temperature. This trend is not surprising as it is known that metal nitrate decomposition temperatures decrease with increasing metal cation charge density.[61] The higher charge density of Al^{3+} polarizes the nitrate ions, weakening N–O bond strengths and lowering decomposition temperatures for the Al-rich films.

TGA provides insight into the decomposition of the bulk precursor powders, but these measurements do not necessarily relate to the corresponding evolution of thin films due to differences in sample geometry, mass transport, and evaporation rates.[62,63] Nevertheless, TGA is useful for providing approximate temperature ranges at which decomposition events take place and for correlating how these change with metal composition.

FTIR allows a direct measurement of water and nitrate content in ZAO films as a function of annealing temperature (Fig. 2). These spectra indicate that significant water (~3500 cm^{-1})[64] and nitrate (~1280 and 1460 cm^{-1})[31,65] are retained in films annealed at 200 °C (Fig. 2a). Al-rich films generally contain less nitrate, consistent with TGA data of bulk powders. Water is fully removed from films of all compositions by 400 °C (Fig. S1†), and nitrate is effectively removed by 500 °C (Fig. 2b).

Peaks indicative of Al–O (~600 to 900 cm^{-1})[31] and Zr–O (~415 cm^{-1})[41] are observed for the pure AlO_y and ZrO_y films, respectively. The intensity of these peaks increases for films annealed at higher temperatures, indicating oxide formation is more complete. Significant overlap and broadening of the metal oxide peaks makes identification of Al–O and Zr–O peaks in the mixed composition samples difficult.[41] The loss of water and nitrate, coincident with growth of the oxide peak intensities, suggest that condensation is largely complete by 500 °C. XRR studies (which allow measurement of film thickness and density) also show that densification is complete by 500 °C (Fig. S2 and S3†).

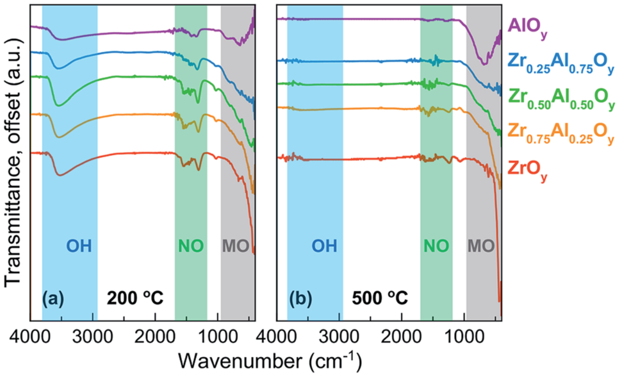

Fig. 2 FTIR spectra of two-coat ZAO films annealed at (a) 200 °C and (b) 500 °C. FTIR spectra of ZAO films annealed at 300 and 400 °C can be found in Fig. S1.†

As discussed above, amorphous metal oxides are preferred for gate oxide applications because grain boundaries in polycrystalline films negatively impact device performance.[3,34] The extent of crystallization as a function of Zr : Al composition and annealing temperature was investigated using GIXRD (Fig. 3a and b). All compositions were amorphous at 400 °C, while ZrO_y is crystalline by 500 °C. ZAO films with compositions of ≥25% Al are amorphous at 500 °C and remain so up to 600 °C. The minimum amount of Al needed to prevent crystallization at 500 °C was 10% Al, although these films crystallize by 600 °C.

For many microelectronic applications, subnanometer surface roughness is essential for optimum device functionality.[66–68] AFM shows ZAO films annealed at 500 °C (Fig. 4) are remarkably smooth (root-mean-square roughness (R_{rms}) < 1 nm). AlO_y films, in particular, are exceptionally smooth with

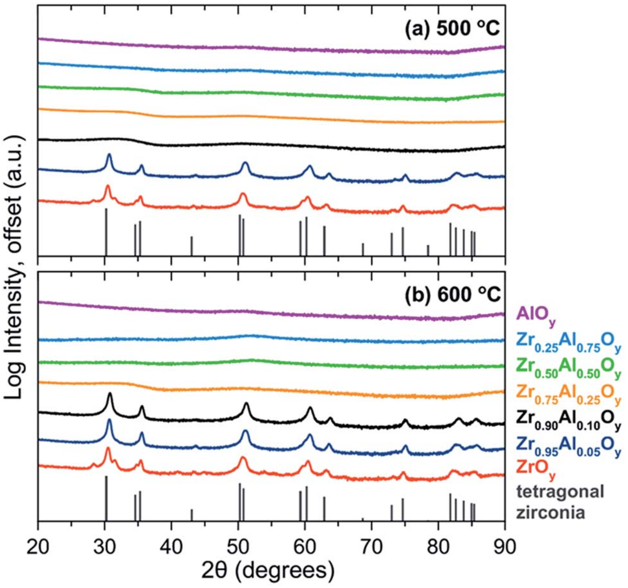

Fig. 3 GIXRD of single-coat ZAO films annealed at (a) 500 °C and (b) 600 °C. The tetragonal zirconia phase (ICSD 66781)[69] is plotted for reference.

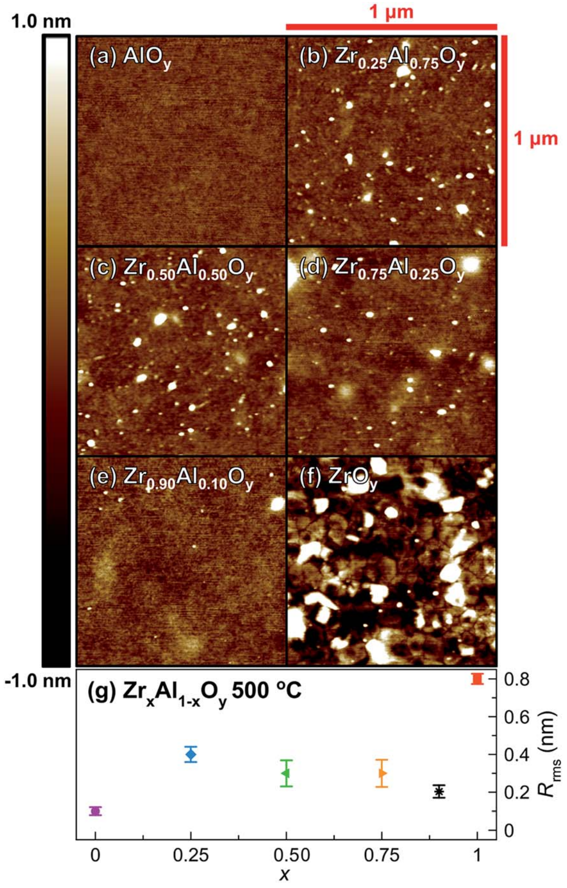

Fig. 4 Representative AFM images of single-coat (a) AlO$_y$, (b) Zr$_{0.25}$Al$_{0.75}$O$_y$, (c) Zr$_{0.50}$Al$_{0.50}$O$_y$, (d) Zr$_{0.75}$Al$_{0.25}$O$_y$, (e) Zr$_{0.90}$Al$_{0.10}$O$_y$, and (f) ZrO$_y$ films annealed at 500 °C (1 μm^2 area) and (g) corresponding surface roughness values. Error bars were determined using measurements taken from three separate 1 μm^2 areas on the same film.

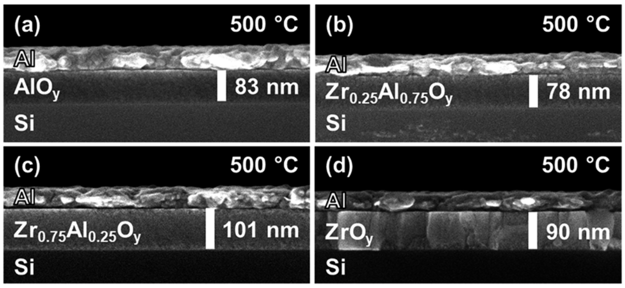

Fig. 5 SEM cross-sectional images of two-coat (a) ZrO$_y$, (b) Zr$_{0.75}$Al$_{0.25}$O$_y$, (c) Zr$_{0.25}$Al$_{0.75}$O$_y$, and (d) AlO$_y$ films annealed at 500 °C.

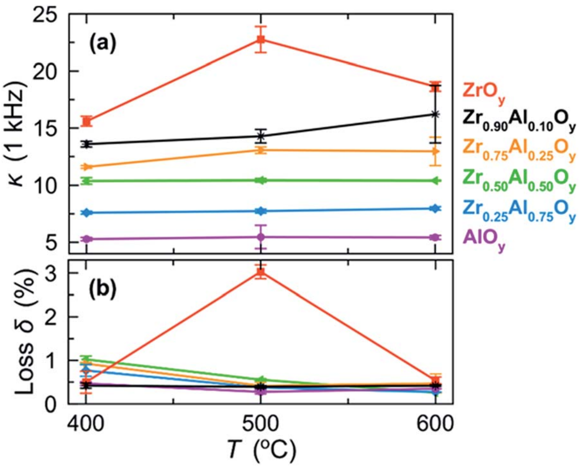

Fig. 6 (a) Dielectric constants (κ) measured at 1 kHz and (b) corresponding loss tangents (loss δ) for MIS devices fabricated from two-coat (~100 nm) ZAO films annealed at various temperatures. Error bars were determined using measurements taken from three separate batches of ZAO-based MIS devices. A plot of κ and loss δ as a function of frequency for ZAO-based MIS devices fabricated at 500 °C can be found in Fig. S4.†

$R_{rms} \approx 0.1$ nm (Fig. 4a). ZAO films with varying Zr : Al ratios are still quite smooth with $R_{rms} \approx 0.2$–0.4 nm (Fig. 4b–e). In contrast, ZrO$_y$ films are significantly rougher ($R_{rms} \approx 0.8$ nm). This increased roughness is likely associated with crystallization observed by GIXRD; indeed, crystallites are apparent in AFM images (Fig. 4f).

Cross-sectional SEM shows the morphology of stacked, two-coat ZAO films incorporated into MIS devices (Fig. 5). Amorphous ZAO films are dense and homogeneous, with no signs of interfacial roughness (Fig. 5a–c). In the case of crystalline ZrO$_y$, large columnar grains are observed (Fig. 5d).

MIS devices were fabricated from two-coat ZAO films, and dielectric properties were examined by impedance spectroscopy (Fig. 6 and S4†). Dielectric constants (1 kHz) increase with increasing Zr content, ranging from 5.4 (AlO$_y$) to 18.6 (ZrO$_y$) for films annealed at 600 °C. We attribute the large increases in dielectric constants and batch-to-batch variations for ZrO$_y$ films annealed at 500 °C and Zr$_{0.90}$Al$_{0.10}$O$_y$ films annealed at 600 °C to the onset of crystallization (see Fig. 4). Generally, loss tangents were low, indicating minimal deviation from ideal capacitance (Fig. 6b).

Although it is difficult to directly compare properties of materials deposited using different precursors and thermal treatments,[63] the dielectric constants reported here are within the range of values reported in the literature. In a previous sol–gel study, Zr$_{0.10}$Al$_{0.90}$O$_y$ films annealed between 250 and 350 °C for 2 h exhibited dielectric constants of 8.4 to 11.8.[42] Although these values are larger than those reported here, they compare well to dielectric constant of Zr$_{0.25}$Al$_{0.75}$O$_y$ films we prepared at 200 °C ($\kappa \approx 12$) and 300 °C ($\kappa \approx 10$). We do not include data for samples annealed at these low temperatures in Fig. 6 because FTIR data (Fig. 2 and S1†) indicate that these films contain residual polarizable water and nitrate, which can inflate dielectric constant values and lead to sample-to-sample variations.[53] In a separate ultrasonic spray pyrolysis study, ZAO films with similar compositions and annealing temperatures (475 °C) are also in the range of those reported here.[39]

J–*E* measurements were conducted to assess the effects of Zr : Al composition on breakdown fields and leakage current densities of ZAO-based MIS devices processed at 500 °C (Fig. 7). In general, Zr$_x$Al$_{1-x}$O$_y$ devices experience catastrophic breakdown (defined as $I > 100$ mA) and loss of insulating behaviour at lower

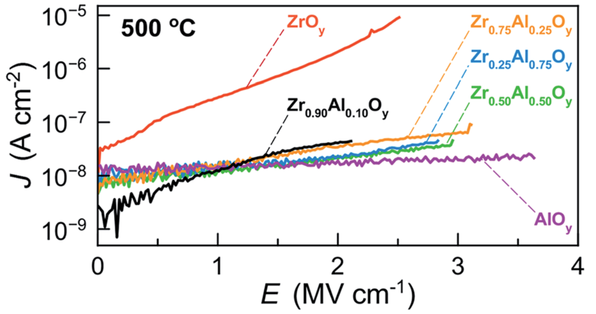

Fig. 7 Representative *JE* data for MIS devices made from two-coat ZAO films (~100 nm) annealed at 500 °C.

electric fields when $x \geq 0.90$ (2.0 to 2.5 MV cm^{-1}). In addition to lower breakdown voltages, batch-to-batch variation for $Zr_{0.90}Al_{0.10}O_y$ devices was high, suggesting the formation of microcrystallites beneath the detection limit of GIXRD for these films. In contrast, devices fabricated from more Al-rich $Zr_xAl_{1-x}O_y$ films ($x \leq 0.25$) experience breakdown at higher electric fields (~3 MV cm^{-1}), with AlO_y devices breaking down at ~3.7 MV cm^{-1}.

Additionally, ZrO_y-based MIS devices display the highest leakage current densities at all electric fields, in agreement with the relatively high loss δ measured for ZrO_y-based devices annealed at 500 °C (Fig. 6b). We attribute this to the formation of crystallites and the presence of grain boundaries in films annealed at this temperature.[34] Notably, incorporation of Al significantly decreases the leakage current densities of ZAO-based devices at all electric fields. $Zr_xAl_{1-x}O_y$ films with $0.25 \leq x \leq 0.90$ show similar low leakage current densities, while AlO_y films exhibit the lowest leakage current densities. Together, the MIS characterization suggests that $Zr_{0.75}Al_{0.25}O_y$ displays the optimal balance of a high dielectric constant and low leakage current densities.

Conclusions

We report an all-inorganic aqueous deposition route to variable composition high-κ zirconium aluminium oxide films with sub-nm surface roughness and tunable properties. Residual nitrate and water are fully removed from ZAO films by 500 °C, and incorporation of Al ≥10% effectively suppresses crystallization of the tetragonal zirconia phase up to 500 °C. Dielectric constants increase with increasing Zr content, and films with Al >10% exhibit low leakage current densities. For the composition range studied, the combination of high dielectric constant and low leakage current densities makes $Zr_{0.75}Al_{0.25}O_y$ a promising candidate for microelectronic applications.

Conflicts of interest

There are no conflicts of interest to declare.

Acknowledgements

This work was funded by the National Science Foundation Center for Sustainable Materials Chemistry (CSMC, Grant CHE-1606982). We gratefully acknowledge the use of UO CAMCOR High-Resolution and Nanofabrication Facility, which is supported by grants from the W. M. Keck Foundation, the M. J. Murdock Charitable Trust, ONAMI, the Air Force Research Laboratory (agreement FA8650-05-1-5041), NSF (Awards 0923577 and 0421086), and the University of Oregon. The authors thank Matthew G. Kast, Julija Vinckevičiūtė, and Paul N. Plassmeyer for preliminary studies and helpful discussions. This research was conducted as part of the 2016 CSMC Summer Materials Research Training (SMaRT) program and we thank the staff, graduate student mentors, and undergraduate participants.

References

1 J. Robertson, *Rep. Prog. Phys.*, 2006, **69**, 327–396.
2 E. Fortunato, P. Barquinha and R. Martins, *Adv. Mater.*, 2012, **24**, 2945–2986.
3 G. D. Wilk, R. M. Wallace and J. M. Anthony, *J. Appl. Phys.*, 2001, **89**, 5243–5275.
4 J. P. Maria, D. Wicaksana, A. I. Kingon, B. Busch, H. Schulte, E. Garfunkel and T. Gustafsson, *J. Appl. Phys.*, 2001, **90**, 3476–3482.
5 K. Kukli, K. Forsgren, M. Ritala, M. Leskelä, J. Aarik and A. Hårsta, *J. Electrochem. Soc.*, 2001, **148**, F227–F232.
6 G. Adamopoulos, S. Thomas, P. H. Wöbkenberg, D. D. C. Bradley, M. A. McLachlan and T. D. Anthopoulos, *Adv. Mater.*, 2011, **23**, 1894–1898.
7 L. Xifeng, X. Enlong and Z. Jianhua, *IEEE Trans. Electron Devices*, 2013, **60**, 3413–3416.
8 J. H. Park, Y. B. Yoo, K. H. Lee, W. S. Jang, J. Y. Oh, S. S. Chae and H. K. Baik, *ACS Appl. Mater. Interfaces*, 2013, **5**, 410–417.
9 Y. M. Park, A. Desai, A. Salleo and L. Jimison, *Chem. Mater.*, 2013, **25**, 2571–2579.
10 J. Jang, R. Kitsomboonloha, S. L. Swisher, E. S. Park, H. Kang and V. Subramanian, *Adv. Mater.*, 2013, **25**, 1042–1047.
11 A. Liu, G. X. Liu, H. H. Zhu, F. Xu, E. Fortunato, R. Martins and F. K. Shan, *ACS Appl. Mater. Interfaces*, 2014, **6**, 17364–17369.
12 G. X. Liu, A. Liu, F. K. Shan, Y. Meng, B. C. Shin, E. Fortunato and R. Martins, *Appl. Phys. Lett.*, 2014, **105**, 113509.
13 C. Zhu, A. Liu, G. Liu, G. Jiang, Y. Meng, E. Fortunato, R. Martins and F. Shan, *J. Mater. Chem. C*, 2016, **4**, 10715–10721.
14 W. He, W. Xu, Q. Peng, C. Liu, G. Zhou, S. Wu, M. Zeng, Z. Zhang, J. Gao, X. Gao, X. Lu and J.-M. Liu, *J. Phys. Chem. C*, 2016, **120**, 9949–9957.
15 C. Avis and J. Jang, *J. Mater. Chem.*, 2011, **21**, 10649–10652.
16 T. Lim, D. Kim and S. Ju, *Appl. Phys. Lett.*, 2013, **103**, 13107.
17 Y. Liu, P. Guan, B. Zhang, M. L. Falk and H. E. Katz, *Chem. Mater.*, 2013, **25**, 3788–3796.
18 J. H. Park, K. Kim, Y. B. Yoo, S. Y. Park, K.-H. Lim, K. H. Lee, H. K. Baik and Y. S. Kim, *J. Mater. Chem. C*, 2013, **1**, 7166–7174.
19 P. K. Nayak, M. N. Hedhili, D. Cha and H. N. Alshareef, *Appl. Phys. Lett.*, 2013, **103**, 33518.
20 H. J. Ha, S. W. Jeong, T.-Y. Oh, M. Kim, K. Choi, J. H. Park and B.-K. Ju, *J. Phys. D: Appl. Phys.*, 2013, **46**, 235102.
21 E. J. Bae, Y. H. Kang, M. Han, C. Lee and S. Y. Cho, *J. Mater. Chem. C*, 2014, **2**, 5695–5703.

22 L. Y. Liang, H. T. Cao, Q. Liu, K. M. Jiang, Z. M. Liu, F. Zhuge and F. L. Deng, *ACS Appl. Mater. Interfaces*, 2014, **6**, 2255–2261.

23 G. Huang, L. Duan, G. Dong, D. Zhang and Y. Qiu, *ACS Appl. Mater. Interfaces*, 2014, **6**, 20786–20794.

24 H. Wang, T. Sun, W. Xu, F. Xie, L. Ye, Y. Xiao, Y. Wang, J. Chen and J. Xu, *RSC Adv.*, 2014, **4**, 54729–54739.

25 Y. S. Rim, H. Chen, Y. Liu, S.-H. Bae, H. J. Kim and Y. Yang, *ACS Nano*, 2014, **8**, 9680–9686.

26 R. Branquinho, D. Salgueiro, L. Santos, P. Barquinha, L. Pereira, R. Martins and E. Fortunato, *ACS Appl. Mater. Interfaces*, 2014, **6**, 19592–19599.

27 H. Park, Y. Nam, J. Jin and B.-S. Bae, *RSC Adv.*, 2015, **5**, 102362–102366.

28 R. Branquinho, D. Salgueiro, A. Santa, A. Kiazadeh, P. Barquinha, L. Pereira, R. Martins and E. Fortunato, *Semicond. Sci. Technol.*, 2015, **30**, 24007.

29 H. Tan, G. Liu, A. Liu, B. Shin and F. Shan, *Ceram. Int.*, 2015, **41**, S349–S355.

30 A. Liu, G. Liu, H. Zhu, B. Shin, E. Fortunato, R. Martins and F. Shan, *RSC Adv.*, 2015, **5**, 86606–86613.

31 W. Xu, H. Wang, F. Xie, J. Chen, H. Cao and J.-B. Xu, *ACS Appl. Mater. Interfaces*, 2015, **7**, 5803–5810.

32 Y. S. Rim, H. Chen, T.-B. Song, S.-H. Bae and Y. Yang, *Chem. Mater.*, 2015, **27**, 5808–5812.

33 W. Xu, M. Long, T. Zhang, L. Liang, H. Cao, D. Zhu and J.-B. Xu, *Ceram. Int.*, 2017, **43**, 6130–6137.

34 K. Jiang, J. T. Anderson, K. Hoshino, D. Li, J. F. Wager and D. A. Keszler, *Chem. Mater.*, 2011, **23**, 945–952.

35 J. Zhu and Z. G. Liu, *Microelectron. Eng.*, 2003, **66**, 849–854.

36 Y. Li, J. Zhu, H. Liu and Z. Liu, *Microelectron. Eng.*, 2006, **83**, 1905–1911.

37 D. Zhou, U. Schroeder, G. Jegert, M. Kerber, S. Uppal, R. Agaiby, M. Reinicke, J. Heitmann and L. Oberbeck, *J. Appl. Phys.*, 2009, **106**, 44104.

38 D. Zhou, U. Schroeder, J. Xu, J. Heitmann, G. Jegert, W. Weinreich, M. Kerber, S. Knebel, E. Erben and T. Mikolajick, *J. Appl. Phys.*, 2010, **108**, 124104.

39 M. Bizarro, J. C. Alonso and A. Ortiz, *J. Electrochem. Soc.*, 2005, **152**, F179.

40 M. Bizarro, J. C. Alonso and A. Ortiz, *Mater. Sci. Semicond. Process.*, 2006, **9**, 1090–1096.

41 P. Vitanov, A. Harizanova, T. Ivanova, C. Trapalis and N. Todorova, *Mater. Sci. Eng., B*, 2009, **165**, 178–181.

42 W. Yang, K. Song, Y. Jung, S. Jeong and J. Moon, *J. Mater. Chem. C*, 2013, **1**, 4275–4282.

43 S. R. Thomas, P. Pattanasattayavong and T. D. Anthopoulos, *Chem. Soc. Rev.*, 2013, **42**, 6910–6923.

44 S. Park, C.-H. Kim, W.-J. Lee, S. Sung and M.-H. Yoon, *Mater. Sci. Eng., R*, 2017, **114**, 1–22.

45 Q. Fan, B. McQuillin, A. K. Ray, M. L. Turner and A. B. Seddon, *J. Phys. D: Appl. Phys.*, 2000, **33**, 2683–2686.

46 Z. Wang, U. Helmersson and P.-O. Käll, *Thin Solid Films*, 2002, **405**, 50–54.

47 J. T. Anderson, C. L. Munsee, C. M. Hung, T. M. Phung, G. S. Herman, D. C. Johnson, J. F. Wager and D. A. Keszler, *Adv. Funct. Mater.*, 2007, **17**, 2117–2124.

48 S. T. Meyers, J. T. Anderson, D. Hong, C. M. Hung, J. F. Wager and D. A. Keszler, *Chem. Mater.*, 2007, **19**, 4023–4029.

49 M. Alemayehu, J. E. Davis, M. Jackson, B. Lessig, L. Smith, J. D. Sumega, C. Knutson, M. Beekman, D. C. Johnson and D. A. Keszler, *Solid State Sci.*, 2011, **13**, 2037–2040.

50 K. Jiang, S. T. Meyers, M. D. Anderson, D. C. Johnson and D. A. Keszler, *Chem. Mater.*, 2013, **25**, 210–214.

51 R. P. Oleksak, W. F. Stickle and G. S. Herman, *J. Mater. Chem. C*, 2015, **3**, 3114–3120.

52 A. Nadarajah, M. Z. B. Wu, K. Archila, M. G. Kast, A. M. Smith, T. H. Chiang, D. A. Keszler, J. F. Wager and S. W. Boettcher, *Chem. Mater.*, 2015, **27**, 5587–5596.

53 P. N. Plassmeyer, K. Archila, J. F. Wager and C. J. Page, *ACS Appl. Mater. Interfaces*, 2015, **7**, 1678–1684.

54 K. M. Norelli, P. N. Plassmeyer, K. N. Woods, B. A. Glassy, C. C. Knutson, M. Beekman and C. J. Page, *Solid State Sci.*, 2016, **55**, 8–12.

55 K. N. Woods, T.-H. Chiang, P. N. Plassmeyer, M. G. Kast, A. C. Lygo, A. K. Grealish, S. W. Boettcher and C. J. Page, *ACS Appl. Mater. Interfaces*, 2017, **9**, 10897–10903.

56 K. M. Kim, C. W. Kim, J. S. Heo, H. Na, J. E. Lee, C. B. Park, J.-U. Bae, C.-D. Kim, M. Jun, Y. K. Hwang, S. T. Meyers, A. Grenville and D. A. Keszler, *Appl. Phys. Lett.*, 2011, **99**, 242109.

57 S. W. Smith, W. Wang, D. A. Keszler and J. F. Conley, *J. Vac. Sci. Technol., A*, 2014, **32**, 41501.

58 M. G. Kast, E. A. Cochran, L. J. Enman, G. Mitchson, J. Ditto, C. Siefe, P. N. Plassmeyer, A. L. Greenaway, D. C. Johnson, C. J. Page and S. W. Boettcher, *J. Am. Chem. Soc.*, 2016, **138**, 16800–16808.

59 M. Wormington, C. Panaccione, K. M. Matney and D. K. Bowen, *Philos. Trans. R. Soc., A*, 1999, **357**, 2827–2848.

60 K. H. Kim, Z. Akase, T. Suzuki and D. Shindo, *Mater. Trans.*, 2010, **51**, 1080–1083.

61 S. Yuvaraj, L. Fan-Yuan, C. Tsong-Huei and Y. Chuin-Tih, *J. Phys. Chem. B*, 2003, **107**, 1044–1047.

62 P. Roura, J. Farjas, H. Eloussifi, L. Carreras, S. Ricart, T. Puig and X. Obradors, *Thermochim. Acta*, 2015, **601**, 1–8.

63 S. R. Wood, K. N. Woods, P. N. Plassmeyer, D. A. Marsh, D. W. Johnson, C. J. Page, K. M. Ø. Jensen and D. C. Johnson, *J. Am. Chem. Soc.*, 2017, **139**, 5607–5613.

64 H. A. Al-Abadleh and V. H. Grassian, *Langmuir*, 2003, **19**, 341–347.

65 R. A. Nyquist, C. L. Putzig, M. A. Leugers and R. O. Kagel, *The Handbook of Infrared and Raman Spectra of Inorganic Compounds and Organic Salts*, Academic Press, San Diego, CA, USA, 1997.

66 Y. Jung, R. J. Kline, D. A. Fischer, E. K. Lin, M. Heeney, I. McCulloch and D. M. DeLongchamp, *Adv. Funct. Mater.*, 2008, **18**, 742–750.

67 J.-M. Lee, B.-H. Choi, M.-J. Ji, J.-H. Park, J.-H. Kwon and B.-K. Ju, *Semicond. Sci. Technol.*, 2009, **24**, 55008.

68 N. Alimardani, E. W. Cowell III, J. F. Wager, J. F. Conley Jr, D. R. Evans, M. Chin, S. J. Kilpatrick and M. Dubey, *J. Vac. Sci. Technol., A*, 2012, **30**, 01A113.

69 B. Bondars, G. Heidemane, J. Grabis, K. Laschke, H. Boysen, J. Schneider and F. Frey, *J. Mater. Sci.*, 1995, **30**, 1621–1625.